



Real-time study of the interplay between phase formation and stress evolution at the $W_{1-x}Si_x/a$ -Si interface

Bärbel Krause ^{*}*Institut für Photonenforschung und Synchrotronstrahlung (IPS), [Karlsruher Institut für Technologie](#), D-76021 Karlsruhe, Germany*Clarisse Furgeaud,[†] Cédric Mastail, Anny Michel, Salomé Parent [‡], and Gregory Abadias *Institut Pprime, Département Physique et Mécanique des Matériaux, UPR 3346 CNRS, Université de Poitiers, SP2MI, 86073 Poitiers, France*Andrea Resta, Alessandro Coati , Yves Garreau [§], and Alina Vlad *Synchrotron SOLEIL, L'Orme des Merisiers, Départementale 128, 91190 Saint Aubin, France*

(Received 31 May 2024; accepted 4 September 2024; published 1 October 2024)

Nanoscale $W_{1-x}Si_x$ layers with different Si content were deposited by magnetron sputtering on amorphous silicon layers. The structure and stress evolution during deposition were monitored *in situ* and in real time. Thus, it was possible to disentangle different origins of stress built-up (interface formation, phase formation, grain growth, and texture) on the nanoscale. It was found that the bcc phase with a composition-dependent texture forms at low Si content (less than 10% Si), but only above a critical thickness. At intermediate Si content (13.9% and 16.5% Si), or low Si content and low thicknesses ($\lesssim 4.5$ nm), the β phase with A15 structure and coexisting phases (bcc or amorphous) form, while a single, amorphous phase is observed at high Si content ($\gtrsim 22\%$ Si). An A15 formation driven by impurities (O,C,N) was excluded by combined *in situ* x-ray photoelectron spectroscopy and *ex situ* x-ray diffraction measurements on a second sample series. *Ab initio* calculations of substitutional bcc and A15 $W_{1-x}Si_x$ alloys support the formation of A15 at higher Si content. The A15-containing interlayer should be taken into account when discussing the superconductivity of W/Si multilayers. The stress evolution during deposition of $W_{1-x}Si_x$ was correlated with the microstructure evolution, and compared to similar observations for $Mo_{1-x}Si_x$. Due to the crystalline phase (bcc/A15) and bcc texture ([111] and [110]) competition, the structure formation of $W_{1-x}Si_x$ shows a higher complexity. This explains the wide range of stress states (from tensile to compressive) observed after deposition of $W_{1-x}Si_x$. Nanoscale W-Si based stress-compensation layers could be employed for tailoring the stress state of nonepitaxial semiconductor devices.

DOI: [10.1103/PhysRevMaterials.8.103401](https://doi.org/10.1103/PhysRevMaterials.8.103401)

I. INTRODUCTION

Over the years, the research on the material system W-Si was driven by various application fields, including W/Si x-ray multilayer optics [1,2], oxidation-resistant coatings for the walls of fusion reactors [3], and superconducting thin films [4]. The emerging fields of quantum cryptography [5–9] and spintronics [10–13] have revived the interest in ultrathin W-Si

films. Recent studies focus mainly on metastable phases such as A15 and amorphous W-Si [8,14]. Experimental and theoretical studies identified the tungsten A15 phase as the origin of a giant spin-Hall effect [10–13], and the amorphous W-Si phase with a Si content around 20% was found to give the highest normal-to-superconducting transition temperature of the W-Si system [4,15].

At room temperature, the thermodynamically stable phases in the W-Si system are W-bcc, the silicides W_5Si_3 and WSi_2 , and elemental silicon with diamond structure [16,17]. The W-A15 phase (also called β -W) is metastable and can be transformed by annealing or electron irradiation into W-bcc (α -W) [18,19]. In agreement with experimental studies, *ab initio* calculations indicate that the addition of light elements, such as oxygen, nitrogen, and carbon, stabilizes the A15 phase. It was also proposed that a similar structural control can be obtained by the addition of Si and Ge. In contrast to the light elements, which are occupying interstitial sites of the A15 structure [20], it is assumed that Si and Ge occupy substitutional sites [21,22].

Early studies reported a Si- or Ge-induced phase sequence from A15 via bcc to amorphous [4]. Unfortunately, this is also the phase sequence proposed for increasing concentrations

^{*}Contact author: baerbel.krause@kit.edu[†]Present address: CNRS, INSA Lyon, Ecole Centrale de Lyon, Université Claude Bernard Lyon 1, CPE Lyon, INL, UMR5270, 69130 Ecully, France.[‡]Also at Institut für Photonenforschung und Synchrotronstrahlung (IPS), Karlsruher Institut für Technologie, D-76021 Karlsruhe, Germany.[§]Also at Laboratoire Matériaux et Phénomènes Quantiques, Université Paris Cité, Paris, France.

Published by the American Physical Society under the terms of the [Creative Commons Attribution 4.0 International](#) license. Further distribution of this work must maintain attribution to the author(s) and the published article's title, journal citation, and DOI.

of typical impurities such as O, C, and N, but information about the elemental composition was not provided. For W/Si multilayers, a thickness-dependent transition from A15 to bcc was found [1], but also here contamination effects cannot be excluded. To overcome this problem, we have performed an *in situ* and real-time study of the structure formation at the $W_{1-x}Si_x$ /a-Si interface, combined with *ab initio* calculations probing the relative stability of the experimentally observed structures. Simultaneous x-ray reflectivity (XRR), x-ray diffraction (XRD), and optical stress measurements were performed during sputter deposition, focusing on early growth stages and interface formation. As already demonstrated for several metal/amorphous semiconductor interfaces [23–25], this experimental approach gives access to the structural evolution during thin-film growth, which can then be correlated with the stress evolution during layer formation. The structure/composition relationship was verified by combining *in situ* x-ray photoelectron spectroscopy (XPS) reference measurements of as-deposited surfaces, and *ex situ* XRD measurements.

The main questions we address in the following are (1) Which Si content is required for stabilizing different $W_{1-x}Si_x$ phases? (2) How does the Si content affect the thickness-dependent structure formation close to the $W_{1-x}Si_x$ /a-Si interface? and (3) Which impact has the composition-dependent structure formation on the stress evolution during thin-film growth? As will be shown, we confirm experimentally and theoretically that Si can stabilize the A15 structure. The intermixing is also responsible for a transitional A15 stabilization during early growth stages. The average stress during later growth stages can be either tensile or compressive, depending on the structure evolution, and can thus serve as an indicator for the phase formation close to the interface.

II. METHODS

A. Experimental methods

All samples studied in this work were deposited in a sputter chamber dedicated for *in situ* x-ray experiments [25,26]. For the real-time experiments during thin-film deposition, the chamber with a base pressure of 3×10^{-6} Pa was installed at the beamline SIXS of the synchrotron SOLEIL. a-Si/ $W_{1-x}Si_x$ /a-Si trilayers, consisting of a 7-nm-thick Si buffer layer, 35–45 nm $W_{1-x}Si_x$, and a 3.5-nm-thick Si capping layer, were deposited with Si contents x in the range 0–0.35. The Si(100) substrates with a thickness of 100 μ m were covered by native oxide. Si was deposited by rf magnetron sputtering at a target-substrate distance $d_{T-S} = 129$ mm and tungsten by dc magnetron sputtering at $d_{T-S} = 184$ mm. Both targets had a diameter of 50 mm. During deposition, the Ar flux of 1.2 sccm resulted in a pressure of 0.37 Pa. a-Si was deposited with a target power of 60 W. For Si deposited at 60 W, the growth rate was 0.0144 ± 0.0004 nm/s. For W deposited at 40 W, a growth rate of 0.062 ± 0.002 nm/s was obtained. $W_{1-x}Si_x$ alloys with a Si content up to 35% were deposited using cosputtering, the Si content being controlled by the target powers $P(W) = 15$ –40 W and $P(Si) = 0$ –90 W. A second set of samples, reference layers on solvent-cleaned 1-mm-thick Si(100) substrates (covered by

native oxide), was deposited at the Karlsruhe Institute of Technology (KIT), where the same growth chamber was docked to a UHV cluster system with base pressure 2×10^{-8} Pa. The chemical composition of these samples was determined by *in situ* XPS before capping (see Appendix A, Fig. 10). For two real-time samples (0.8% and 8.6% Si), the composition was interpolated; all other growth conditions were verified experimentally. After capping, *ex situ* laboratory XRD measurements were performed with a Smartlab diffractometer (Rigaku), ensuring the reproducibility of the phase formation for both sample series (real-time and XPS reference samples; see Appendix C).

The thin-film formation during sputter deposition was monitored *in situ* by a combination of simultaneous real-time synchrotron (x-ray reflectivity, x-ray diffraction) and optical stress measurements. Details about this experimental approach can be found in Refs. [23,24]. The XRD measurements give information about phase formation, grain growth, and texture. The XRR result was used to determine the deposition rate [27]. The synchrotron experiments were performed at a photon energy of 10 keV ($\lambda = 0.124$ nm) and an incident angle $\alpha_i = 2^\circ$. During deposition, the reflected signal was measured by a point detector at a distance of 1035 mm, and the diffracted signal in the 2θ range 23° – 37° was recorded with an XPAD two-dimensional pixel detector at a distance of 305 mm. The real-time measurements were supplemented by XRD maps recorded before and after deposition. The sample curvature during deposition was monitored using a multiple laser beam optical stress sensor (k-Space Associates, USA). The film force per unit width, (F/w) , which is equal to the stress-thickness product $\sigma * d$, was derived from the change in curvature $\Delta\kappa$ using the Stoney equation. From this, the instantaneous change of the stress signal with deposited layer thickness, i.e., the incremental stress $\sigma_i = \frac{\partial(F/w)}{\partial d}$, was determined.

B. Theoretical methods

The phase formation of W-Si alloys was theoretically studied by *ab initio* calculations of the bcc and A15 phases as a function of the Si content. The calculations were carried out in the framework of the density functional theory (DFT). The Kohn-Sham equations were solved by using the projector augmented wave method [28] implemented in the Vienna simulation *ab initio* package (VASP 5.2) [29,30]. The exchange-correlation contribution to the electronic energy was calculated with the generalized-gradient approximation (GGA) developed by Perdew, Burke, and Ernzerhof [31]. We used the standard potentials for W and Si, which treat the 6s and 5d, and the 2s and 2p states as valence electrons, and we consider the spin polarization. The plane wave cut-off energy was fixed at 325 eV. The Brillouin-zone integration was carried out using a gamma centered grid with a spaced mesh of $9 \times 9 \times 9$ points to evaluate the total energy to within an accuracy of 10^{-5} eV/atom. Complete relaxation of the atomic positions was assumed for atomic forces less than 0.001 eV/Å on each atom.

For pure W, the simulation of the bcc phase was based on a $3 \times 3 \times 3$ supercell with 54 W atoms, the A15 phase was simulated using a $2 \times 2 \times 2$ supercell with 64 W atoms. Substitutional and interstitial phases with different Si content

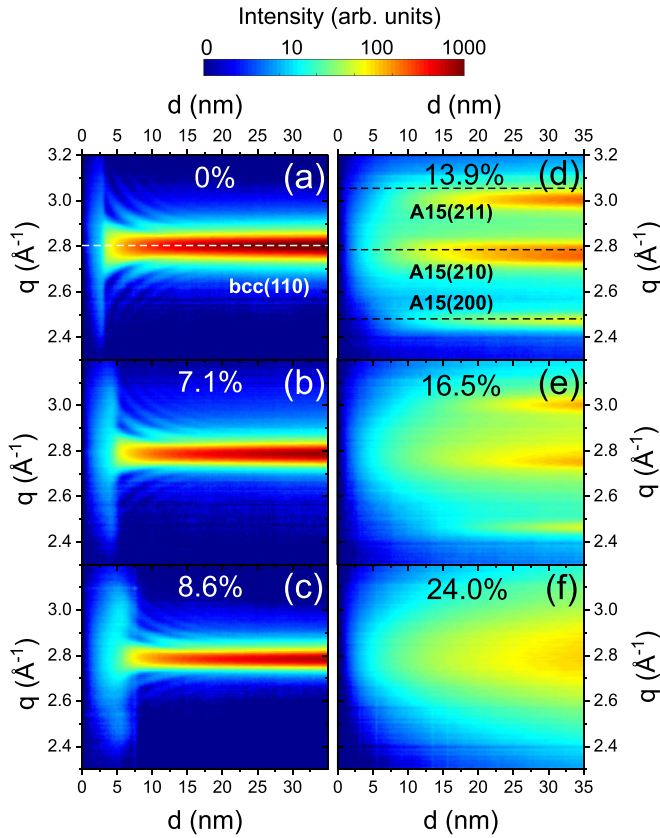


FIG. 1. Composition-dependent XRD signal during deposition of 35 nm $W_{1-x}Si_x$ on a-Si (logarithmic scale). (a)–(c) show XRD maps representative of the bcc formation at low Si content ($x \leq 10\%$), (d) and (e) show the evolution in the intermediate (A15-dominated) range, and (f) shows the typical signal of a highly disordered layer at high Si content ($x \gtrsim 22\%$). The expected peak positions of bcc-W and A15 are indicated by dashed lines in (a) and (d).

were calculated. The tested interstitial configurations were highly unfavorable, therefore we focus in this work on substitutional configurations. To mimic substitutional $W_{1-x}Si_x$ solid solutions with different Si fractions x , we employed the special quasirandom structure approach [32]. In this approach, the W-Si alloy is simulated by a random distribution of different elements on the lattice sites. The solid solution configuration was obtained with the ATAT software, using the MCSQS code [33]. The meaningfulness of the calculation results was ensured by comparison with literature.

III. RESULTS

A. Composition-dependent phase formation

Real-time growth studies during deposition of $W_{1-x}Si_x$ on a-Si were performed in the composition range 0%–24% Si. Based on the time-dependent XRD signal, three composition ranges with different phase formation were identified. Figures 1(a)–1(f) give examples for the evolution of the radial XRD signal with increasing film thickness (q/d maps). The data were integrated along the section of the diffraction rings indicated in Fig. 2(c). All measurements are shown

as a function of the nominal layer thickness d calculated from the deposition rate. For low Si content (less than 10% Si), the initially broad intensity distribution changes suddenly into the bcc(110) peak. The transition occurs at a concentration-dependent critical thickness, d_c , as already observed for Mo-Si, and can be explained with a thickness-dependent crystallization of the already deposited material [23]. Such a recrystallization is not observed for medium and high Si content. In the medium Si range (13.9% and 16.5% Si), three reflections appear, as expected for A15. The texture (see below) and the broadening of the central ring [see Appendix B, Fig. 11(c)] evidence a coexisting bcc fraction. For high Si content ($\gtrsim 22\%$ Si), a continuously increasing, broad intensity distribution is found, indicating a highly disordered, amorphous or nanocrystalline structure. This broad intensity distribution overlaps also with the Bragg peaks observed at 16.5% Si, indicating a coexisting disordered phase already at intermediate Si content.

The Si content affects the orientation of the highly textured bcc phase: Figs. 2(a)–2(d) compare XRD diffraction rings in different composition regimes, recorded after deposition. In the low Si range, the bcc texture evolves with increasing Si content from [110] [Fig. 2(a)] to [111] [Fig. 2(b)]. The respective intensity maxima along the bcc(110)/A15(210) diffraction ring (“bcc/A15 ring”) are indicated by red arrows. In the medium Si range [Fig. 2(c)], the bcc[111] reflections are still visible. The coexisting A15 texture cannot be identified, due to the width of the orientation distribution in combination with a high multiplicity of the studied reflections. The broad ring indicating a highly disordered structure is shown in Fig. 2(d) for a Si content of 24.0%. The evolution of the bcc texture is better visible in Fig. 2(e), which compares the integrated intensity along the bcc/A15 ring for different Si contents, plotted as a function of the angle χ to the surface normal. The gray region is not accessible in grazing incidence geometry. For the bcc[110], a bcc(110) maximum is expected, $\chi = 0^\circ$ and $\chi = \pm 60^\circ$, while bcc[111] should cause intensity maxima at $\chi = \pm 35^\circ$. With increasing Si content, the bcc[110] peak at $\chi = -60^\circ$ decreases (black arrow), while the peaks around $\pm 35^\circ$ (green arrows) increase.

Our results demonstrate that the Si content controls the thickness-dependent phase and texture formation of W-Si films. The phase and texture after deposition were confirmed by *ex situ* XRD measurements (Appendix C). Surprisingly, the postgrowth measurements at 16.5% Si show a comparatively large bcc fraction, compared to the minor fraction found during deposition. This indicates that a metastable A15 phase transforms with time into bcc. In the next section, the observed phases will be rationalized by *ab initio* calculations.

B. *Ab initio* calculations for the understanding of the structure evolution

To understand the experimentally observed phase formation, *ab initio* calculations of bcc and A15 substitutional phases with different Si content were performed. Table I presents the simulation results for random solid solutions with bcc and A15 structure: the total energy, E , of the cell, the total energy per atom, E^* , the Si content in percent, and the number of Si atoms inserted in the cell, n_{Si} . In

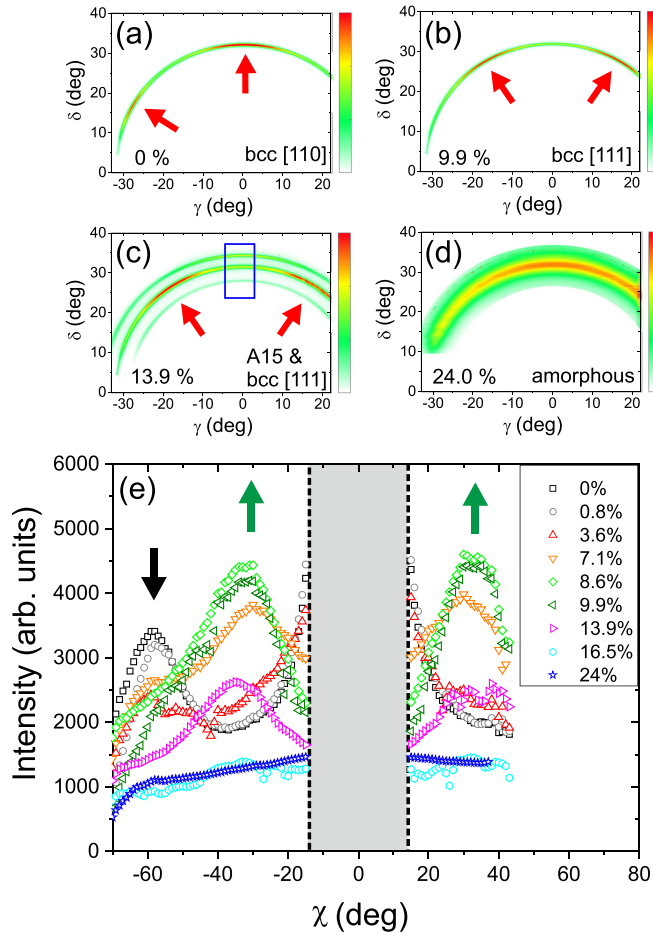


FIG. 2. (a)–(d) Composition-dependent intensity distribution along characteristic diffraction rings of the bcc and the A15 phase, measured *in situ* (after sample capping) for $W_{1-x}Si_x$ with $x = 0, 9\%, 13.9\%$, and 24% . The blue rectangle in (c) indicates the region monitored during deposition. (e) Integrated intensity along the diffraction ring at $q = 2.8 \text{ \AA}^{-1}$ (“bcc/A15 ring”). The angle χ is defined with respect to the surface normal, and the gray area indicates a region in reciprocal space that is not accessible at grazing incidence. The arrows indicate peak positions expected for the bcc[110] (black) and the bcc[111] (green) textures.

agreement with literature results [19,20,34], the A15 tungsten phase is metastable with $E_{W,A15}^*$ 85 meV higher than $E_{W,bcc}^*$. Our optimized bcc lattice constant, $d_{W,bcc} = 3.172 \text{ \AA}$, as well as the A15 bulk lattice parameter, $d_{W,A15} = 5.06 \text{ \AA}$, agree well with other DFT-GGA simulated [35,36] and experimental [37] results found in the literature. The calculated bulk modulus of 304.4 GPa, obtained for the W-bcc phase, is in agreement with typical experimental values in range of 295–312 GPa (He and Duffy. [38], and references therein). For W-A15, our calculations give a bulk modulus of 302.2 GPa.

Interpolating the E^* data, we find that the substitutional bcc phase has a higher stability up to a Si content of 28%. At higher Si content, the substitutional A15 phase is preferred. The mixing enthalpy

$$\Delta H_{\text{mix}}^{\text{bcc/A15}} = \frac{1}{n_{\text{cell}}} [E - (n_W E_W^{\text{bcc/A15}} + n_{\text{Si}} E_{\text{Si}}^{\text{bcc/A15}})], \quad (1)$$

TABLE I. Total energy, E , and energy per atom, E^* , for substitutional W-Si solid solutions. The assumed Si content is given in percent and as the number of lattice sites occupied by silicon atoms.

Cell	Si (%)	n_{Si}	E (eV)	E^* (eV/atom)
bcc	0.00	0	−702.82	−13.015
	1.85	1	−694.83	−12.867
	3.70	2	−686.93	−12.720
	5.56	3	−678.87	−12.572
	11.11	6	−655.25	−12.134
	16.67	9	−630.42	−11.674
	20.37	11	−614.47	−11.379
	25.93	14	−591.48	−10.953
	33.33	18	−559.71	−10.365
	50.00	27	−492.61	−9.122
	66.67	36	−422.88	−7.831
	74.07	40	−390.74	−7.236
A15	100.00	54	−264.61	−4.900
	0.00	0	−827.56	−12.931
	1.56	1	−819.94	−12.812
	3.13	2	−812.05	−12.688
	4.68	3	−804.09	−12.564
	6.25	4	−796.18	−12.440
	12.50	8	−765.30	−11.958
	18.75	12	−733.97	−11.468
	25.00	16	−704.13	−11.002
	31.25	20	−674.84	−10.544
	50.00	32	−584.75	−9.137
	68.75	44	−490.05	−7.657
	75.00	48	−458.61	−7.166
	100.00	64	−309.12	−4.830

and the excess enthalpy

$$\Delta H_{\text{ex}}^{\text{bcc/A15}} = \frac{1}{n_{\text{Si}}} \left(E - \frac{n_W}{n_{\text{cell}}} E_W^{\text{bcc/A15}} \right) \quad (2)$$

are different ways to represent the impact of Si substitution on the energetics of the W-Si phases. The parameters n_{cell} , $n_W = n_{\text{cell}} - n_{\text{Si}}$, and $E_W^{\text{bcc/A15}}$ are the number of atoms in the cell, the number of tungsten atoms in the cell, and the total energy for pure W and Si in the bcc or A15 structure. Both thermodynamic quantities were calculated from the simulation results (Fig. 3). The mixing enthalpy evolution [Fig. 3(a)] is in good agreement with literature data calculated for ordered compounds [17,39]. The substitution of W by Si is energetically favorable for both structures, but W-Si alloys with A15 structure show a greater relative stability [Fig. 3(a)]. This was also confirmed by Chattaraj *et al.* [35] who calculated the cohesive energy of ordered W_3Si in the bcc (−7.471 eV/atom) and A15 (−7.631 eV/atom) phases. For comparison: our computed cohesive energy for substitutional W-Si with the same composition is −7.39 eV/atom (bcc) and −7.40 eV/atom (A15). These values were calculated assuming the reference values $E_W = -4.526 \text{ eV}$ and $E_{\text{Si}} = -0.806 \text{ eV}$ for isolated atoms in the gas phase.

The excess enthalpy of A15 and bcc is similar [Fig. 3(b), filled symbols]. However, when the excess enthalpy of A15 is calculated with respect to the bcc ground state, i.e., with E_W^{bcc} (open symbols), it becomes obvious that the A15

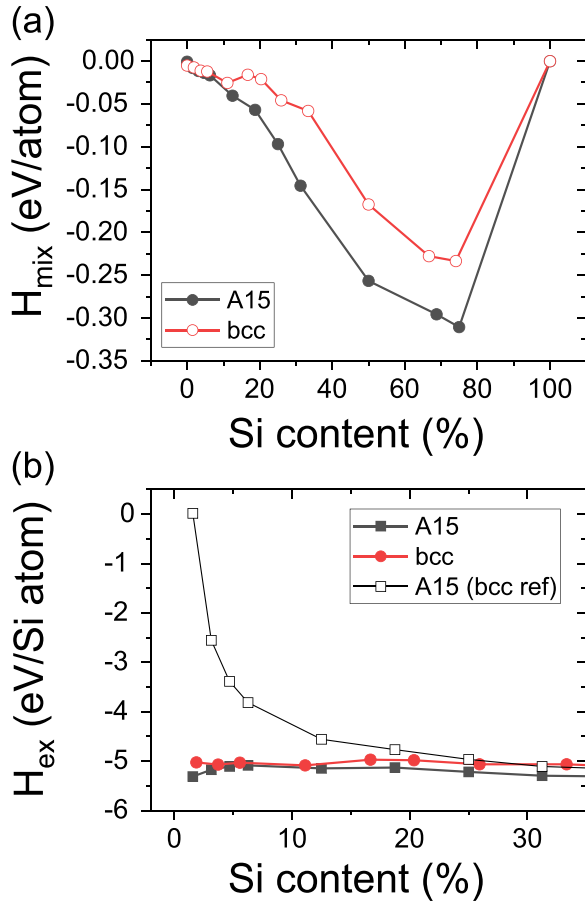


FIG. 3. (a) W-Si mixing enthalpy and (b) excess enthalpy of the bcc and the A15 structure (filled symbols). For comparison, the A15 excess enthalpy is plotted also with respect to the bcc ground state of tungsten (open symbols).

structure is highly unfavorable below 10% Si. Above 10% Si, the difference in excess energies of bcc and A15 (with respect to the bcc ground state) is comparatively small. In this range, the relative stability of A15 increases continuously, and above 28% Si A15 is the preferred phase (as already found from E^*).

In agreement with the experimental results, the *ab initio* calculations confirm that W-Si alloys with A15 structure are favorable for high Si contents. However, experimentally we observe the A15 phase already at 13.9% Si, which is far below the theoretical value of 28%. Under experimental conditions, which are far from thermodynamic equilibrium, metastable phases can form. The excess energy with respect to the tungsten ground state indicates that metastable A15 and bcc solid solutions are likely to coexist above a Si content of about 10%. This is also in agreement with the aging effects observed for 16.5% Si, where the dominant A15 phase observed during deposition was later partially converted to bcc.

C. Stress-structure relationship: Recrystallization

After discussing the relative stability of bcc and A15 W-Si solid solutions, we now come to the stress accumulation during thin-film formation which is crucial for the long-term stability of the $W_{1-x}Si_x$ films. Figure 4 visualizes the

stress/structure relationship in the low Si region for $x = 7.1\%$, obtained during deposition. The stress evolution is represented by the F/w curve (central panel, top) and its derivative σ_i (central panel, bottom). It covers the (I) interface formation, (II) growth before recrystallization, (III) recrystallization, and (IV) growth after recrystallization (indicated in the σ_i plot). The positions ②, ④, and ⑥ mark the extrema of F/w (i.e., $\sigma_i = 0$ GPa; black crosses). The positions ①, ③, and ⑤ are prominent positions of σ_i , indicated by blue stars. As an indicator for the structure evolution, XRD line scans at these positions were extracted from the simultaneously measured XRD map [Fig. 2(b)]. Data shown on the left side were recorded before the recrystallization process and the data on the right during the recrystallization process. The line scans reveal the formation of A15 nanocrystallites close to the interface. The position and intensity of the central peak indicate coexisting bcc nanocrystallites. During early growth stages, the peak width is too large to separate these fractions. Therefore, the XRD signal of the A15/bcc nanocrystallites was fitted using three Lorentzian peaks with the same peak width. During recrystallization, the intensity of the three Lorentzian peaks decreases, and a narrow bcc(110) component arises. This component was fitted assuming coherent scattering of oriented crystallites with a narrow size distribution [24].

During interface formation (region I), the incremental stress is tensile ($\sigma_i > 0$). The shoulder at $d \approx 1$ nm [position (1)] is close to the interlayer thickness reported for pure W [1,40,41]. The A15/bcc nanocrystal formation in region II is accompanied by an increasingly compressive stress, which is correlated with the grain size. The average grain size, estimated from the fitted peak width, increases simultaneously from about 2 to 3 nm. This compressive region is followed by a tensile stress increase during recrystallization. Starting from position (3), σ_i increases while the initially formed nanocrystals transform to large bcc(110) crystallites. Throughout the tensile step the average size of the bcc crystallites is always close to the deposited WSi thickness: The average size of the bcc(110) nanocrystals is 4.80 ± 0.03 nm at position (4), 5.13 ± 0.04 nm at position (5), and reaches 6.0 ± 0.5 nm at position (6). This agrees with similar observations for Mo-Si, which will be discussed later. In the following, we will detail the impact of the Si content on the stress evolution, including the interface region and the W-Si growth up to a thickness of several tens of nanometers.

D. Stress-structure relationship: Composition

Figures 5(a) and 5(c) summarize the evolution of F/w for different Si content, and the simultaneously recorded bcc/A15 peak intensity, I_{XRD} , extracted from the XRD maps plotted in Fig. 1. The respective signals close to the WSi/a-Si interface (gray areas) are enlarged in Figs. 5(b) and 5(d). The F/w curves in the low Si range show the characteristic stress evolution described above, with an interface-related tensile increase, a subsequent compressive range during nanocrystal formation, and a tensile step due to recrystallization. The F/w maximum at $d \approx 1$ nm decreases with increasing Si content. In agreement with the XRD results, the tensile jump occurs only for low Si content (up to 9.9%), where recrystallization was observed. The deposited thickness at position

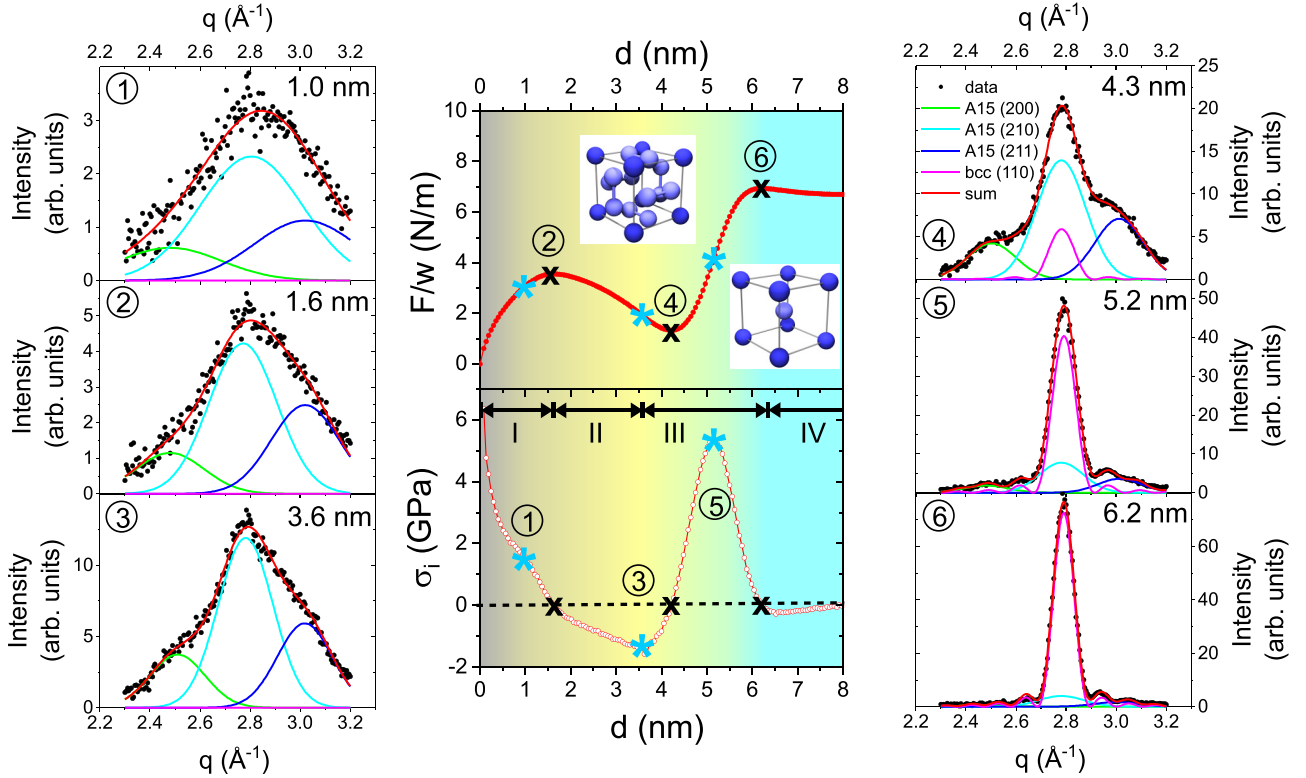


FIG. 4. Correlation between the evolution of F/w and the XRD intensity distribution during sputter deposition of $W_{1-x}Si_x/a-Si$, shown for a silicon content of 7.1%. F/w and its derivative, the incremental stress σ_i , are shown in the center of the figure. The extrema of F/w (black crosses), the prominent positions of σ_i (blue stars), and the structure formation regimes I–IV are indicated. The background color highlights the interface region (gray), the A15 region (yellow), and the bcc region (blue). The respective structures are shown as insets. The corresponding XRD signals are shown on both sides (data points). The results of a peak fit including the A15 and the bcc phase are shown as lines (for details see text).

(3) in Fig. 4 is a good measure for the onset of recrystallization. As shown in Fig. 6(a), the critical thickness for recrystallization increases almost linearly with increasing Si content from 2.5 nm (pure W) to 4.2 nm for 9.9% Si. As an indicator for the composition-dependent recrystallization, Fig. 6(b) compares the crystallization-induced change of F/w and I_{XRD} (see Fig. 4) as a function of d_c . The increasing σ_i after position (3) is associated with the recrystallization. Due to the superposed, and still increasing compressive contribution, however, the difference between the positions (4) and (6) is a better approximation for the step heights ΔI_{XRD} and $\Delta F/w$. For higher Si content, the tensile jump occurs at higher d_c , reflecting the delayed recrystallization. $\Delta F/w$ increases with increasing Si content, while ΔI_{XRD} remains nearly unchanged (see Sec. IV B).

As an indicator for the stress evolution during later growth, Fig. 6(c) shows F/w and I_{XRD} after 30 nm deposition. For low Si content ($x < 10\%$), F/w is positive and decreases with increasing Si content. I_{XRD} decreases similarly. The XRD signal reflects the decreasing fraction of bcc[110], suggesting that the tensile stress during later growth is also related to this texture fraction. For $x > 10\%$, F/w is negative, with an extremely low value at 13.9% Si.

This can be better understood from the σ_i evolution shown in Figs. 7(a) (early growth stages) and 7(b) (up to $d = 35$ nm). The compressive stress is always related to the crystalline A15/bcc fraction. For $x < 10\%$ Si and $d > 1.5$ nm,

the increasingly compressive σ_i was attributed to the presence of A15/bcc crystallites before recrystallization. For 13.9% Si this trend continues up to $\sigma_i = -2.3$ GPa at 20 nm, in agreement with the large volume fraction of A15/bcc evidenced by the XRD peaks in Fig. 1(d). For 16.5% Si, the A15/bcc fraction is much lower, and the XRD peaks emerge later. Consequently, σ_i decreases only from -490 to -810 MPa at $d = 30$ nm. At 24.0% Si, no long-range order is found, and σ_i remains at -490 MPa.

IV. DISCUSSION

A. Phase formation during growth

Figure 8 summarizes the crystalline phases detected in $W_{1-x}Si_x$ films with different thickness and composition. The crystalline phases found in thick (30 nm) W-Si layers are bcc at low Si content ($x \lesssim 10\%$), and coexisting A15 and bcc at intermediate Si content. Below a critical thickness and at low Si content, a mixed A15/bcc phase forms close to the W/Si interface. This phase recrystallizes once the composition-dependent critical thickness, d_c , is reached. In the intermediate Si range, the recrystallization is suppressed, and the A15/bcc crystallites coexist with a disordered phase. The disordered fraction dominates during early growth, and increases with increasing Si content. At high Si content ($x \gtrsim 22\%$), no crystalline fraction is observed in the studied thickness range.

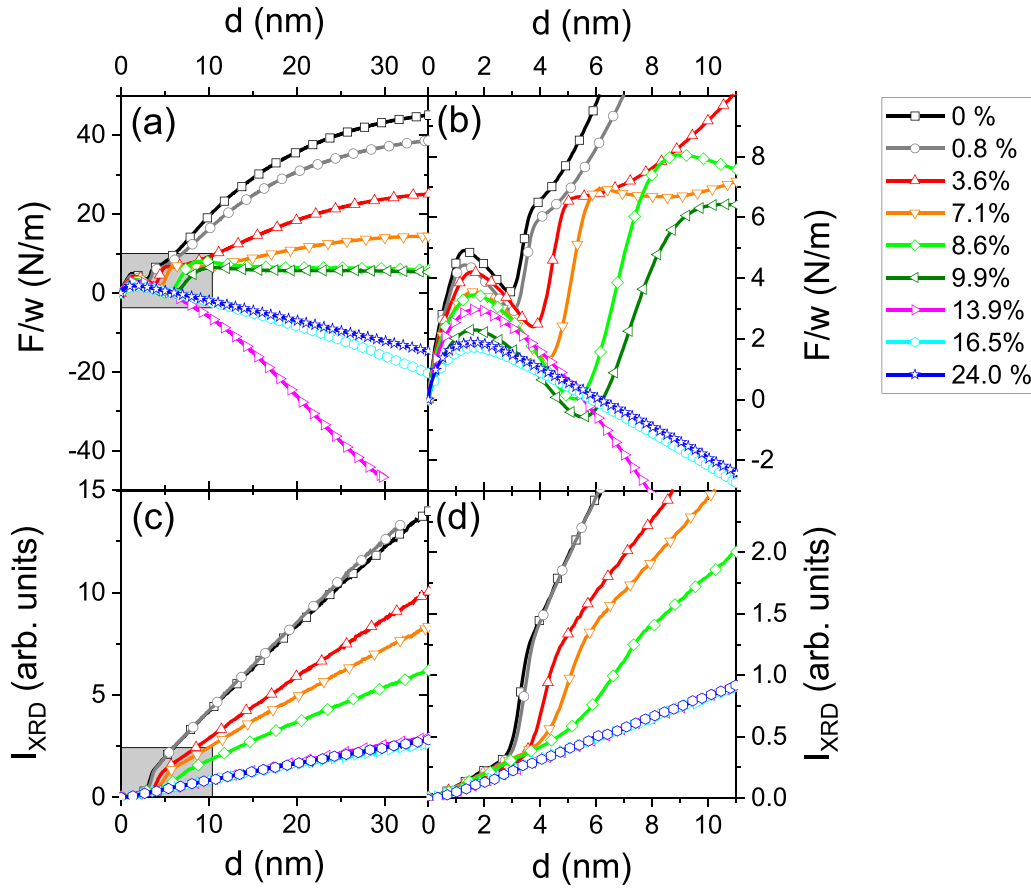


FIG. 5. Composition-dependent evolution of the force per unit width (F/w) during deposition of (a) 35 nm $W_{1-x}Si_x$ on a-Si and (b) zoom into the gray area close to the $W_{1-x}Si_x/a-Si$. (c) and (d) Simultaneously measured XRD signal, I_{XRD} , extracted from the q/t maps shown in Fig. 1 by integration over $q = 2.78 \pm 0.02 \text{ \AA}^{-1}$.

The simulation results confirm that metastable, substitutional W-Si phases are energetically preferred. For pure tungsten, the A15 phase has a higher energy than the bcc ground state. Above a Si content of 28%, the A15 phase becomes stable. However, coexisting A15 and bcc phases are likely for Si contents $\gtrsim 10\%$ Si, where the excess energy of both phases with respect to the tungsten ground state becomes similar. These energetic considerations explain also why the WSi/Si interface promotes the formation of coexisting A15/bcc phases during initial growth: due to the composition gradient at the interfaces, higher local compositions occur and stabilize the A15 phase even during deposition of $W_{1-x}Si_x$ in the bcc (low Si content) range. The observation of metastable (A15 and amorphous) phases with increasing Si content could also indicate that the bcc formation is kinetically hindered. With increasing Si content, the dominant bond type changes from W-W to W-Si, i.e., from metallic to covalent [39]. This reduces the effective adatom mobility, favoring the nucleation of metastable phases.

Our observations are in qualitative agreement with an earlier *ex situ* study of thick W-Si films [4,42]. According to Kondo., the occurrence of A15 coincides with a significant increase of the critical temperature for superconductivity, starting from about 5% Si [4]. Jin *et al.* [15] observe this increase at higher Si content (10% Si), which is in quantitative agreement with our observation of the A15 phase above 9.9%

Si. A stabilization of A15 close to the interface, up to a W thickness of 5.5 nm, was reported by Windt [43]. We propose that this interface-related A15 phase is related to the critical temperature for superconductivity of W/Si multilayers with 1–2 nm W, which increases with an increasing number of periods [44].

Quantitative deviations from literature results, such as an earlier onset of A15 [4,42] and a thicker layer before recrystallization [43], could be due to oxygen contamination (no information available for the reported samples) or silicon depletion during deposition. We found that the bombardment with energetic tungsten atoms, which depends on the growth conditions and the chamber geometry, reduces the Si content (see Appendix A) and is therefore expected to affect the recrystallization process.

B. Phase formation and stress evolution close to the interface:

$W_{1-x}Si_x/a-Si$ vs $Mo_{1-x}Si_x/a-Si$

Our experimental results confirm that the composition- and thickness-dependent phase, texture, and grain size evolution affect the stress accumulation during W-Si deposition. For an intuitive understanding of these effects, Fig. 9 compares the stress evolution during $Mo_{1-x}Si_x/a-Si$ and $W_{1-x}Si_x/a-Si$ interface formation in the low and high Si range. For $Mo_{1-x}Si_x/a-Si$, the low Si range extends up to 20% Si. In

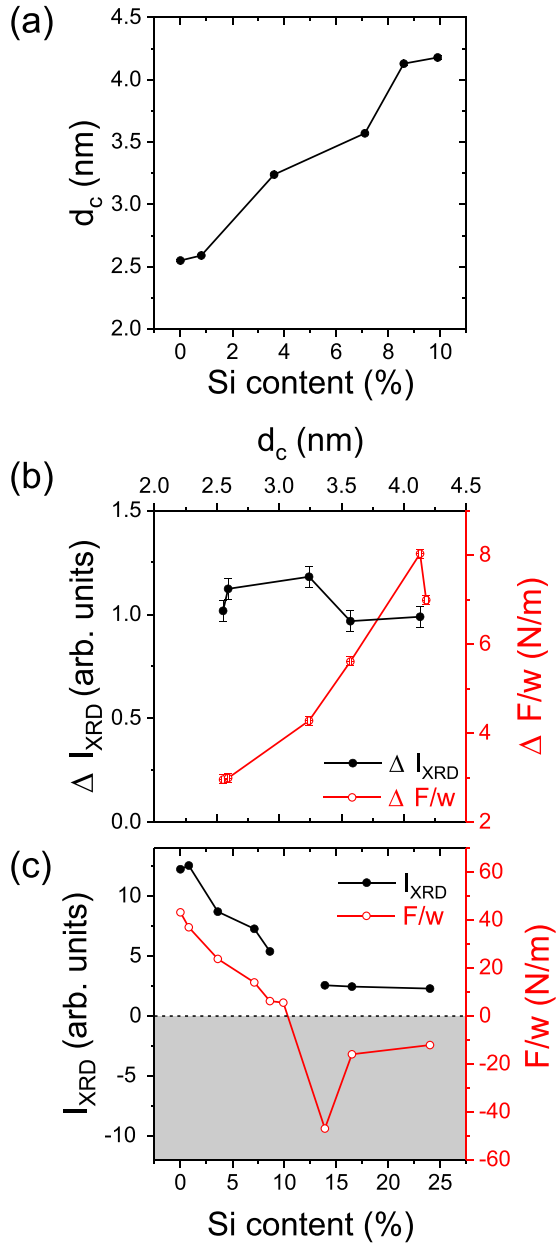


FIG. 6. (a) Critical thickness d_c for the onset of recrystallization. (b) Increase of the diffraction intensity (ΔI_{XRD}) and the force per unit length ($\Delta F/w$) during crystallization. (c) bcc/A15 intensity, I_{XRD} , measured after deposition of 30 nm WSi (dots), and simultaneously measured F/w signal. The values were extracted from the data presented in Fig. 5.

this range, a thickness-dependent crystallization of an amorphous Mo-Si phase into bcc[110] occurs. At $x > 20\%$ (high Si range), an amorphous phase is formed, but no crystallization occurs [23,45]. Compared to $W_{1-x}Si_x$, the structure formation of $Mo_{1-x}Si_x$ is less complex due to the absence of the A15 phase. Before (or in the absence) of recrystallization, all F/w curves of $Mo_{1-x}Si_x$ behave similarly. Reinink *et al.* [46] found a correlation between incremental stress during Mo/a-Si interface formation and the surface chemical composition. In the case of $Mo_{1-x}Si_x$, it seems that this behavior is not affected by the codeposited amount of Si. In contrast to this, the initial

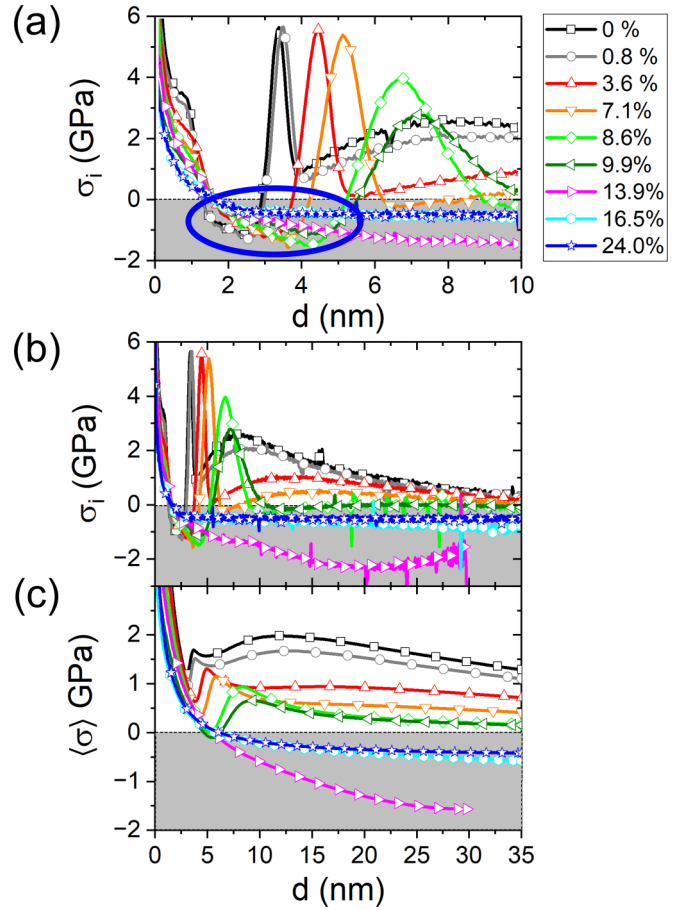


FIG. 7. (a) Incremental stress close to the WSi/a-Si interface. The blue ellipse indicates the thickness range for nanocrystal formation at low Si content ($x < 10\%$ Si). (b) Incremental stress for the entire measurement range. (c) Average stress evolution during W-Si deposition. σ_i and $\langle \sigma \rangle$ were calculated from the F/w data (Fig. 5). Compressive values are highlighted by the gray background.

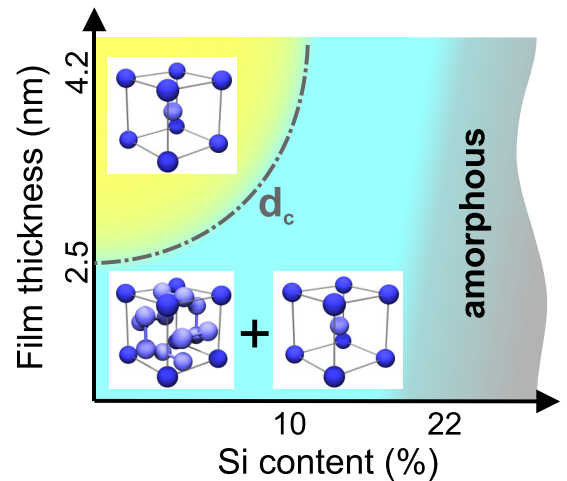


FIG. 8. Crystalline phases detected in $W_{1-x}Si_x$ films with different thickness and composition.

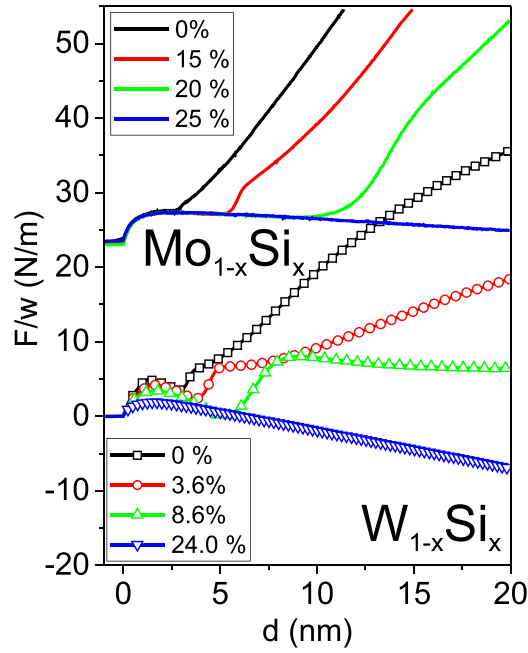


FIG. 9. Evolution of F/w with increasing Si content, measured during deposition of $\text{Mo}_{1-x}\text{Si}_x$ [23] and $\text{W}_{1-x}\text{Si}_x$ on a-Si. Adapted with permission from [23]. Copyright 2016 American Chemical Society.

increase of F/w during $\text{W}_{1-x}\text{Si}_x$ deposition is clearly affected by the composition, likely due to a combination of intermixing and Si depletion. The larger atomic weight of W leads to a higher fraction of backscattered, energetic Ar species [47]. This explains the Si depletion, which was not found for Mo, and is expected to increase the number of point defects. These defects are a possible origin of compressive stress.

The F/w slope after interface formation is clearly related to the atomic ordering. For the $\text{W}_{1-x}\text{Si}_x$ A15/bcc nanocrystals, σ_i is in the range -0.59 to -1.02 GPa [Fig. 7(a)] and decreases with increasing grain size. For both material systems, the tensile increase in the low Si region is proportional to the recrystallized volume. Without A15 formation, the crystallization can be delayed up to a Si content of 20% for $\text{Mo}_{1-x}\text{Si}_x$. Therefore, the amorphous phase can be stabilized up to higher thicknesses, and $\Delta F/w$ can become larger for $\text{Mo}_{1-x}\text{Si}_x$ compared to $\text{W}_{1-x}\text{Si}_x$. After crystallization, the incremental stress of $\text{Mo}_{1-x}\text{Si}_x$ remains tensile, independent of the Si content, but decreases with increasing Si content for $\text{W}_{1-x}\text{Si}_x$. The main difference between both systems is the texture change from bcc[110] to bcc[111], which is found only for $\text{W}_{1-x}\text{Si}_x$. The tensile stress seems to be related to the [110] fraction and can be explained with local epitaxial growth on a strained template [23].

For $\text{Mo}_{1-x}\text{Si}_x$, but not for $\text{W}_{1-x}\text{Si}_x$, the XRD intensity and the F/W curves behave similarly during crystallization. This indicates that both $\text{W}_{1-x}\text{Si}_x$ textures, [110] and [111], form already during crystallization, but the stress relaxation mechanisms during further growth depend on the orientation of the recrystallized templates. In the high Si range, both material systems are stabilized in the amorphous phase, and the stress evolution becomes again similar. The constant

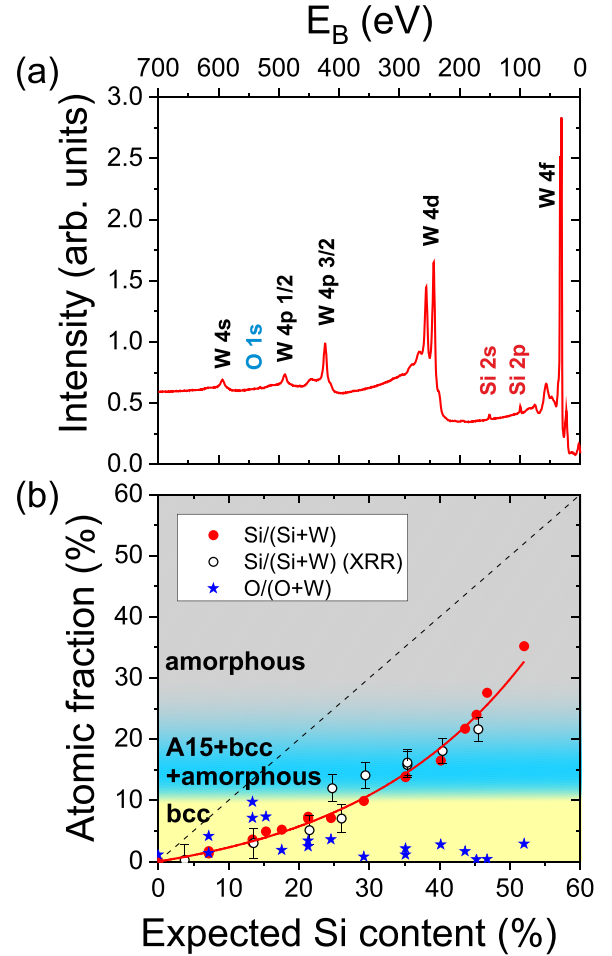


FIG. 10. (a) XPS survey spectrum of a $\text{W}_x\text{Si}_{1-x}$ film with 13.8% Si content (expected Si content 35%). (b) Measured Si content $x = \text{Si}/(\text{Si} + \text{W})$, and O content $y = \text{O}/(\text{O} + \text{W})$, as a function of the expected Si content. The expected Si content was calculated from the atomic fractions determined by XPS. For comparison, x was also calculated from the measured deposition rates of the real-time samples. As a guide to the eye, the Si fraction (XPS) was fitted with an exponential (red line).

incremental stress is compressive ($\sigma_i = -150$ MPa for $\text{Mo}_{1-x}\text{Si}_x$ and $\sigma_i = -490$ MPa for $\text{W}_{1-x}\text{Si}_x$). We attribute the higher compressive stress for $\text{W}_{1-x}\text{Si}_x$ to the Si depletion and point defect formation due to energetic particle bombardment, as discussed above.

After deposition, only the stress averaged over the film thickness is easily accessible. *Ex situ* stress measurements of $\text{W}_{1-x}\text{Si}_x/\text{a-Si}$ systems can be compared with the average stress calculated from the F/w curves [Fig. 7(b)]. Before recrystallization, $\langle \sigma \rangle$ is dominated by the interface contribution and decreases up to the onset of recrystallization. Recrystallization results in a tensile increase of $\langle \sigma \rangle$, which is similar for all compositions. The absolute value of $\langle \sigma \rangle$ is lower for higher Si content, due to the delayed recrystallization. The average stress during later growth ($d > 10$ nm) is an indicator for the phase evolution during growth. The bcc phase is related to a tensile average stress and mixed or amorphous phases to compressive average stress.

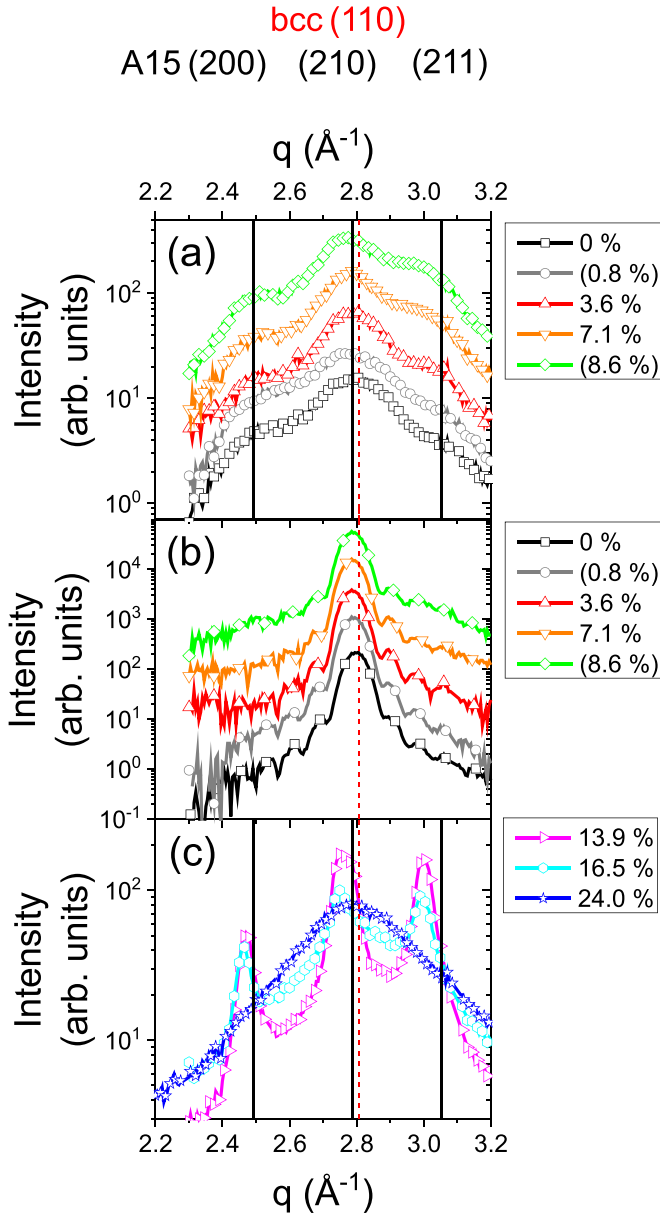


FIG. 11. Line scans extracted close to the onset [position (4); see Fig. 5] and after bcc crystallization ($d = 8$ nm) are shown in (a) and (b). (c) compares line scans extracted at $d = 30$ nm in the bcc/A15 and the amorphous region. The intensity is averaged over 5 s, corresponding to a thickness increase of 0.15–0.3 nm.

V. SUMMARY AND CONCLUSIONS

Our combined real-time XRD and wafer curvature measurements reveal a complex, composition- and thickness-dependent interplay between stress and structure evolution at the $W_{1-x}Si_x/a\text{-Si}$ interface. The formation of metastable, substitutional A15 and bcc phases is in agreement with the relative structural stability of both phases, obtained from *ab initio* calculations. The nucleation and growth of a nanocrystalline A15 and bcc at the interface seems to be related to the critical temperature for superconductivity of W/Si multilayers. Remarkably, the average stress range of $W_{1-x}Si_x/a\text{-Si}$ films above 5 nm covers compressive and

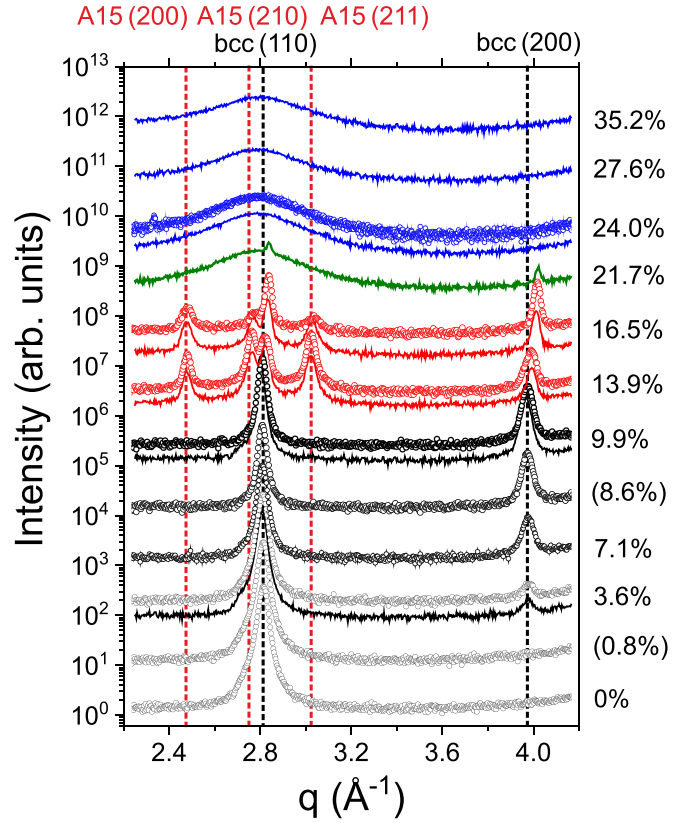


FIG. 12. Composition-dependent specular XRD signal of $a\text{-Si}/W_{1-x}Si_x/a\text{-Si}$ trilayers with different Si content. The intensity of the *ex situ* measurements is plotted in logarithmic scale, with an offset for better visibility. The Si content is indicated on the right side. Data shown as symbols correspond to the real-time samples and data shown as a line plot correspond to the XPS reference samples. The color of the data indicates the composition range: low Si shown in black, medium Si in red, and high Si in blue. The green curve was taken at the transition between medium Si and high Si.

tensile regimes, depending on the interface structure. This has to be taken into account when incorporating these layers in devices. However, it also opens new possibilities for stress design: refractory metals or metal/semiconductor compounds with their comparatively high thermal stability [48–50] have a high potential for tailoring the accumulated stress in nonepitaxial semiconductor devices, thus improving the long-term device stability.

ACKNOWLEDGMENTS

We thank the synchrotron radiation source SOLEIL for the provision of beamtime within the standard Proposal No. 20160160, and acknowledge the support of the synchrotron staff. We are especially grateful for the technical support at the SIXS beamline by Benjamin Voisin. For the technical assistance during preparation of the experiment at the KIT we thank Annette Weißhardt. Furthermore, we acknowledge the general support provided by the staff of the KIT institutes IBPT and IPS. The work also pertains to the French Government programs “Investissements d’Avenir” (EUR INTREE,

Reference No. ANR-18-EURE-0010) and LABEX INTER-ACTIFS (Reference No. ANR-11-LABX-0017-01).

APPENDIX A: CHEMICAL COMPOSITION

The chemical composition was verified by *in situ* XPS characterization of the reference samples, using a non-monochromated XR-50 Mg $K\alpha$ x-ray source and a Phoibos 150 analyzer (SPECS). The overview spectra [Fig. 10(a)] were analyzed with the software CASAXPS. Several peak combinations and background models were tested, with only little influence on the quantitative result. Figure 1(b) summarizes the composition range covered by our experiments, calculated from the areas of Si 2s (linear background), the combined area of the superposed peaks W 4f and W 5p 1/2 (Shirley background), and O 1s (linear background). The depletion rate depends nonlinearly on the Si content of the layer. Demasius *et al.* showed that an oxygen content of at least 10% is required for stabilizing the A15 phase [11]. In our case, y is typically below 3%. The highest y value (near 10%) was found in the bcc range. We conclude that the surface oxygen fraction is not correlated with the observed structure formation but can be explained with postgrowth surface contamination. For some of the samples, we could confirm that they were accidentally stored in the loadlock, which has a base pressure of 10^{-8} mbar, i.e., two orders of magnitude higher than the main UHV cluster, and is frequently exposed to ambient conditions.

APPENDIX B: *IN SITU* XRD—LINE SCANS

Figures 11(a)–11(c) show line scans extracted from the real-time XRD maps (Fig. 1). To reduce the noise, the intensity was averaged over 5 s (corresponding to a thickness increase of 0.15–0.2 nm). For a better understanding

of the low Si range, Fig. 11(a) compares data shortly before the onset of recrystallization (i.e., at different deposited thickness) and Fig. 11(b) after recrystallization (at $d = 8$ nm). The shape of intensity distribution is basically independent of the Si content. The presence of three broad peaks indicates the predominant formation of nanocrystalline A15 before recrystallization. The Bragg peak with size oscillations, observed after recrystallization, indicates the formation of bcc crystallites with a similar size and a narrow size distribution. Figure 11(c) compares line scans for medium (13.9% and 16.5% Si) and high Si content (24% Si), extracted after deposition of 30 nm W-Si. The intensity distribution in the medium Si range can be described as a superposition of the broad intensity distribution characterizing the high Si phase, and three peaks corresponding to the A15 phase. The central peak is broadened compared to the two side peaks, indicating a minor, coexisting bcc phase. The fractions of the individual phases vary with the composition. The disordered fraction is higher for 16.5% Si and the bcc contribution is higher for 13.9% Si.

APPENDIX C: *EX SITU* XRD REFERENCE DATA

The texture evolution with increasing Si content shows also in the *ex situ* XRD scans (Fig. 12). The reference samples were measured within a few days after deposition and the real-time samples were characterized a few weeks after deposition. The bcc(110) peak decreases as expected, while bcc(200) increases. The main texture peak, bcc(111), is outside the scan range. Due to the large peak width, the emerging orientation distribution could also be described as a random fraction with coexisting bcc[111], explaining the presence of the bcc(200) peak. Note that the visibility of small peaks is enhanced by the logarithmic intensity scale.

- [1] D. L. Windt, F. E. Christensen, W. W. Craig, C. Hailey, F. A. Harrison, M. Jimenez-Garate, R. Kalyanaraman, and P. H. Mao, Growth, structure, and performance of depth-graded W/Si multilayers for hard x-ray optics, *J. Appl. Phys.* **88**, 460 (2000).
- [2] K. V. Nikolaev, S. N. Yakunin, I. A. Makhotkin, J. de la Rie, R. V. Medvedev, A. V. Rogachev, I. N. Trunckin, A. L. Vasiliev, C. P. Hendrikx, M. Gateshki, R. W. E. van de Kruijs, and F. Bijkerk, Grazing-incidence small-angle x-ray scattering study of correlated lateral density fluctuations in W/Si multilayers, *Acta Crystallogr., Sect. A: Found. Adv.* **75**, 342 (2019).
- [3] F. Koch and H. Bolt, Self passivating W-based alloys as plasma facing material for nuclear fusion, *Phys. Scr.* **2007**, 100 (2007).
- [4] S. Kondo, Superconducting characteristics and the thermal stability of tungsten-based amorphous thin films, *J. Mater. Res.* **7**, 853 (1992).
- [5] B. Baek, A. E. Lita, V. Verma, and S. W. Nam, Superconducting a-W_xSi_{1-x} nanowire single-photon detector with saturated internal quantum efficiency from visible to 1850 nm, *Appl. Phys. Lett.* **98**, 251105 (2011).
- [6] M. S. Ososky, R. J. Soulen, J. H. Claassen, G. Trotter, H. Kim, and J. S. Horwitz, New insight into enhanced superconductivity in metals near the metal-insulator transition, *Phys. Rev. Lett.* **87**, 197004 (2001).
- [7] F. Marsili, V. B. Verma, J. A. Stern, S. Harrington, A. E. Lita, T. Gerrits, I. Vayshenker, B. Baek, M. D. Shaw, R. P. Mirin, and S. W. Nam, Detecting single infrared photons with 93% system efficiency, *Nat. Photonics* **7**, 210 (2013).
- [8] X. Zhang, A. Engel, Q. Wang, A. Schilling, A. Semenov, M. Sidorova, H.-W. Hübers, I. Charaev, K. Ilin, and M. Siegel, Characteristics of superconducting tungsten silicide W_xSi_{1-x} for single photon detection, *Phys. Rev. B* **94**, 174509 (2016).
- [9] M. V. Sidorova, A. G. Kozorezov, A. V. Semenov, Y. P. Korneeva, M. Y. Mikhailov, A. Y. Devizenko, A. A. Korneev, G. M. Chulkova, and G. N. Goltsman, Nonbolometric bottleneck in electron-phonon relaxation in ultrathin WSi films, *Phys. Rev. B* **97**, 184512 (2018).
- [10] C.-F. Pai, L. Liu, Y. Li, H. W. Tseng, D. C. Ralph, and R. A. Buhrman, Spin transfer torque devices utilizing the giant spin Hall effect of tungsten, *Appl. Phys. Lett.* **101**, 122404 (2012).
- [11] K.-U. Demasius, T. Phung, W. Zhang, B. P. Hughes, S.-H. Yang, A. Kellock, W. Han, A. Pushp, and S. S. P. Parkin, Enhanced spin-orbit torques by oxygen incorporation in tungsten films, *Nat. Commun.* **7**, 10644 (2016).
- [12] E. Derunova, Y. Sun, C. Felser, S. S. P. Parkin, B. Yan, and M. N. Ali, Giant intrinsic spin Hall effect in W₃Ta and other A15 superconductors, *Sci. Adv.* **5**, eaav8575 (2019).

- [13] J. Li, S. Ullah, R. Li, M. Liu, H. Cao, D. Li, Y. Li, and X.-Q. Chen, Topological massive Dirac fermions in β -tungsten, *Phys. Rev. B* **99**, 165110 (2019).
- [14] Q. Hao, W. Chen, and G. Xiao, Beta (β) tungsten thin films: Structure, electron transport, and giant spin Hall effect, *Appl. Phys. Lett.* **106**, 182403 (2015).
- [15] J. Jin, F. Fu, X. Jia, L. Kang, Z. Wang, X. Tu, L. Zhang, B. B. Jin, J. Chen, W. Xu, and P. Wu, Preparation and characterization of ultrathin WSi films for superconducting nanowire single-photon detectors, *IEEE Trans. Appl. Supercond.* **29**, 1 (2019).
- [16] H. Fujiwara, Y. Ueda, A. Awasthi, N. Krishnamurthy, and S. P. Garg, Determination of the standard free energies of formation for tungsten silicides by EMF measurements using lithium silicate liquid electrolyte, *J. Alloys Compd.* **391**, 307 (2005).
- [17] Z. Guo, W. Yuan, Y. Sun, Z. Cai, and Z. Qiao, Thermodynamic assessment of the Si-Ta and Si-W systems, *J. Phase Equilib. Diffus.* **30**, 564 (2009).
- [18] C. L. Chen, T. Nagase, and H. Mori, In situ TEM observations of irradiation-induced phase change in tungsten, *J. Mater. Sci.* **44**, 1965 (2009).
- [19] K. Barmak, J. Liu, L. Harlan, P. Xiao, J. Duncan, and G. Henkelman, Transformation of topologically close-packed β -W to body-centered cubic α -W: Comparison of experiments and computations, *J. Chem. Phys.* **147**, 152709 (2017).
- [20] M. H. F. Sluiter, Interstitials in tetrahedrally close-packed phases: C, N, O, and F in β -tungsten from first principles, *Phys. Rev. B* **80**, 220102(R) (2009).
- [21] Y. Chen, A. N. Kolmogorov, D. G. Pettifor, J.-X. Shang, and Y. Zhang, Theoretical analysis of structural stability of TM_5Si_3 transition metal silicides, *Phys. Rev. B* **82**, 184104 (2010).
- [22] Y. Pan and W. M. Guan, Probing the balance between ductility and strength: Transition metal silicides, *Phys. Chem. Chem. Phys.* **19**, 19427 (2017).
- [23] B. Krause, G. Abadias, A. Michel, P. Wochner, S. Ibrahimkuty, and T. Baumbach, Direct observation of the thickness-induced crystallization and stress build-up during sputter-deposition of nanoscale silicide films, *ACS Appl. Mater. Interfaces* **8**, 34888 (2016).
- [24] B. Krause, G. Abadias, C. Furgeaud, A. Michel, A. Resta, A. Coati, Y. Garreau, A. Vlad, D. Hauschild, and T. Baumbach, Interfacial silicide formation and stress evolution during sputter deposition of ultrathin pd layers on a-Si, *ACS Appl. Mater. Interfaces* **11**, 39315 (2019).
- [25] B. Krause, G. Abadias, D. Babonneau, A. Michel, A. Resta, A. Coati, Y. Garreau, A. Vlad, A. Plech, P. Wochner, and T. Baumbach, In situ study of the interface-mediated solid-state reactions during growth and postgrowth annealing of Pd/a-Ge bilayers, *ACS Appl. Mater. Interfaces* **15**, 11268 (2023).
- [26] B. Krause, S. Darma, M. Kaufholz, H.-H. Gräfe, S. Ulrich, M. Mantilla, R. Weigel, S. Rembold, and T. Baumbach, Modular deposition chamber for *in situ* x-ray experiments during rf and dc magnetron sputtering, *J. Synchrotron Radiat.* **19**, 216 (2012).
- [27] M. Kaufholz, B. Krause, S. Kotapati, M. Köhl, M. F. Mantilla, M. Stüber, S. Ulrich, R. Schneider, D. Gerthsen, and T. Baumbach, Monitoring the thin film formation during sputter deposition of vanadium carbide, *J. Synchrotron Radiat.* **22**, 76 (2015).
- [28] P. E. Blöchl, Projector augmented-wave method, *Phys. Rev. B* **50**, 17953 (1994).
- [29] G. Kresse and J. Furthmüller, Efficient iterative schemes for *ab initio* total-energy calculations using a plane-wave basis set, *Phys. Rev. B* **54**, 11169 (1996).
- [30] G. Kresse and D. Joubert, From ultrasoft pseudopotentials to the projector augmented-wave method, *Phys. Rev. B* **59**, 1758 (1999).
- [31] J. P. Perdew, K. Burke, and M. Ernzerhof, Generalized gradient approximation made simple, *Phys. Rev. Lett.* **77**, 3865 (1996).
- [32] A. Zunger, S.-H. Wei, L. G. Ferreira, and J. E. Bernard, Special quasirandom structures, *Phys. Rev. Lett.* **65**, 353 (1990).
- [33] A. van de Walle, P. Tiwary, M. de Jong, D. Olmsted, M. Asta, A. Dick, D. Shin, Y. Wang, L.-Q. Chen, and Z.-K. Liu, Efficient stochastic generation of special quasirandom structures, *Calphad* **42**, 13 (2013).
- [34] K. Heinola and T. Ahlgren, Diffusion of hydrogen in bcc tungsten studied with first principle calculations, *J. Appl. Phys.* **107**, 113531 (2010).
- [35] A. Chattaraj, A. Kanjilal, and V. Kumar, Ab initio study of the structural stability and Dirac fermion behaviour in A_3B ($\text{A} = \text{Cr, Mo, W}$; $\text{B} = \text{Al, Ga, In, Si, Ge, Sn, Be}$) and W_3M , $\text{M} = \text{Ru, Ta, Re, Os, Ir, Au}$ compounds, *Phys. B (Amsterdam, Neth.)* **646**, 414315 (2022).
- [36] A. Nagakubo, H. T. Lee, H. Ogi, T. Moriyama, and T. Ono, Elastic constants of beta tungsten thin films studied by picosecond ultrasonics and density functional theory, *Appl. Phys. Lett.* **116**, 021901 (2020).
- [37] I. A. Weerasekera, S. I. Shah, D. V. Baxter, and K. M. Unruh, Structure and stability of sputter deposited beta-tungsten thin films, *Appl. Phys. Lett.* **64**, 3231 (1994).
- [38] D. He and T. S. Duffy, X-ray diffraction study of the static strength of tungsten to 69 GPa, *Phys. Rev. B* **73**, 134106 (2006).
- [39] H. Yan, Z. Wei, M. Zhang, and Q. Wei, Exploration of stable stoichiometries, ground-state structures, and mechanical properties of the W-Si system, *Ceram. Int.* **46**, 17034 (2020).
- [40] T. Salditt, D. Lott, T. H. Metzger, J. Peisl, G. Vignaud, P. Hoghoj, O. Schärpf, P. Hinze, and R. Lauer, Interfacial roughness and related growth mechanisms in sputtered W/Si multilayers, *Phys. Rev. B* **54**, 5860 (1996).
- [41] R. V. Medvedev, A. A. Zameshin, J. M. Sturm, A. E. Yakshin, and F. Bijkerk, W/B short period multilayer structures for soft x-rays, *AIP Adv.* **10**, 045305 (2020).
- [42] M. Suzuki, Characterization of silane-reduced tungsten films grown by CVD as a function of si content, *J. Electrochem. Soc.* **137**, 3213 (1990).
- [43] D. L. Windt, Stress, microstructure, and stability of Mo/Si, W/Si, and Mo/C multilayer films, *J. Vac. Sci. Technol., A* **18**, 980 (2000).
- [44] E. Majkova, S. Luby, M. Jergel, H. V. Löhneysen, C. Strunk, and B. George, Superconductivity and critical fields in amorphous tungsten/silicon multilayers, *Phys. Status Solidi A* **145**, 509 (1994).
- [45] A. Fillon, G. Abadias, A. Michel, C. Jaouen, and P. Villechaise, Influence of phase transformation on stress evolution during growth of metal thin films on silicon, *Phys. Rev. Lett.* **104**, 096101 (2010).
- [46] J. Reinink, A. Zameshin, R. W. E. van de Kruijs, and F. Bijkerk, In-situ studies of silicide formation during growth of molybdenum-silicon interfaces, *J. Appl. Phys.* **126**, 135304 (2019).

- [47] Y. Takagi, Y. Sakashita, H. Toyoda, and H. Sugai, Generation processes of super-high-energy atoms and ions in magnetron sputtering plasma, *Vacuum* **80**, 581 (2006).
- [48] I. Nedelcu, R. W. E. van de Kruijs, A. E. Yakshin, and F. Bijkerk, Temperature-dependent nanocrystal formation in Mo/Si multilayers, *Phys. Rev. B* **76**, 245404 (2007).
- [49] W. Knaepen, C. Detavernier, R. V. Meirhaeghe, J. J. Sweet, and C. Lavoie, In-situ x-ray diffraction study of metal induced crystallization of amorphous silicon, *Thin Solid Films* **516**, 4946 (2008).
- [50] W. Knaepen, S. Gaudet, C. Detavernier, R. L. Van Meirhaeghe, J. J. Sweet, and C. Lavoie, In situ x-ray diffraction study of metal induced crystallization of amorphous germanium, *J. Appl. Phys.* **105**, 083532 (2009).